Electronic Supplementary Material (ESI) for Catalysis Science & Technology.

Supplementary Materials for

Developing a Microwave-Driven Reactor for Ammonia Synthesis: Unique Challenges of Microwave Catalysis

Sunjay G Melkote[1*], Pranjali Muley[2, 3], Biswanath Dutta[2, 3], Christina Wildfire[2], Robert Weiss[1], Jianli Hu[4]

[1] Malachite Technologies, Inc., San Francisco, CA, USA

[2] National Energy Technology Laboratory, 3610 Collins Ferry Road, Morgantown, WV 26505 USA

[3] NETL Support Contractor, 3610 Collins Ferry Road, Morgantown, WV 26505, USA

[4] West Virginia University, Morgantown, WV, USA

S1. Reactor, Model, & Diagrams

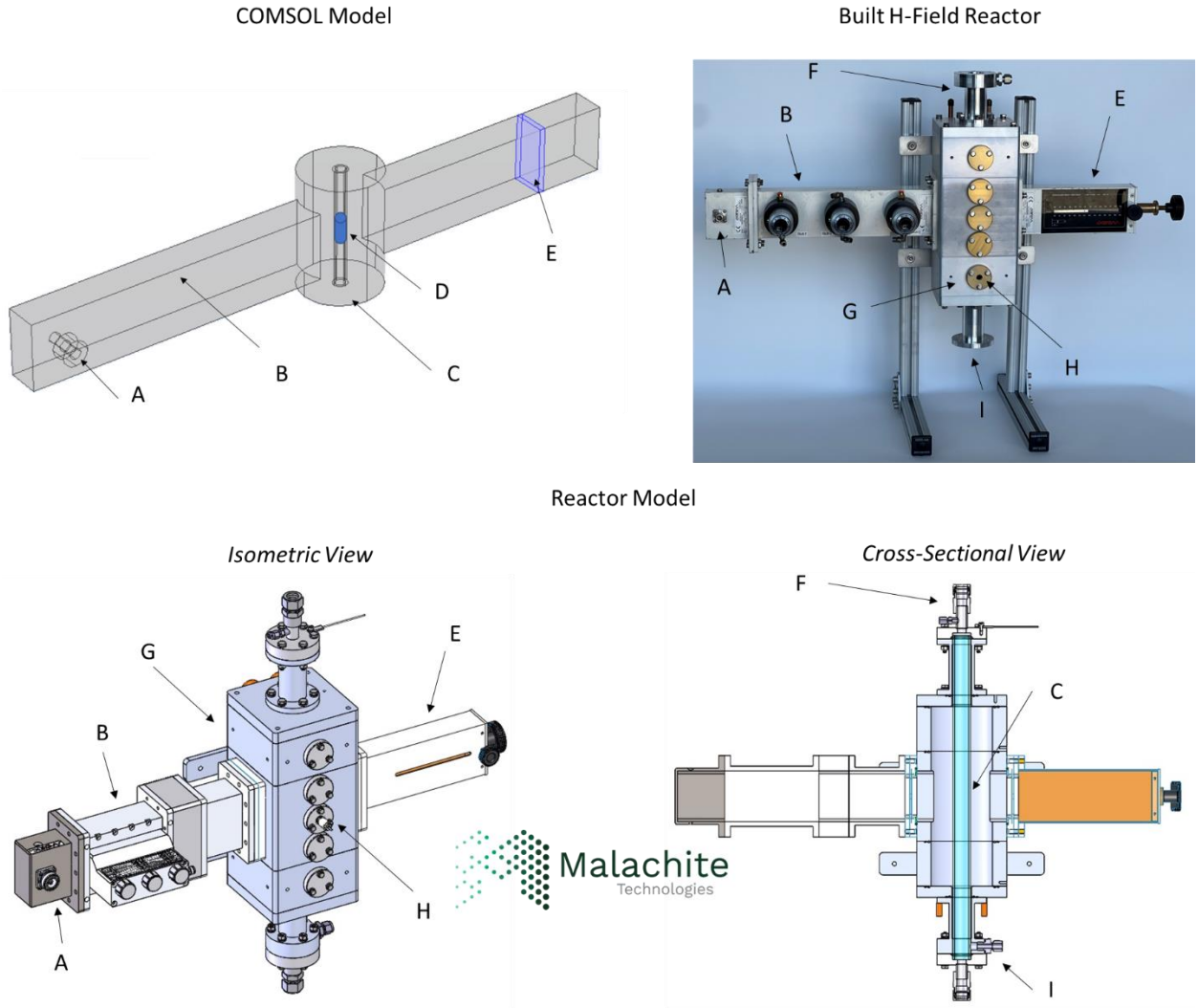

Figure S1. (*top left*) COMSOL-generated model of H-field microwave reactor used for numerical modeling. Matches the (*bottom left*) isometric and (*bottom right*) cross-sectional views of a (*top right*) modular H-field microwave reactor designed by Malachite Technologies, Inc., compatible with an external microwave source. **(A)** Coaxial to waveguide port for solid state or magnetron microwave generators. **(B)** Wave guide with three adjustable stub tuners. **(C)** Quartz tube centered in reactor cavity to house catalyst bed. **(D)** Location of the catalyst bed centered in the quartz tube in the reactor. **(E)** A sliding short circuit to provide optimal microwave tuning. **(F)** Aluminum housing to contain microwave field and serve as secondary containment during high pressure work, sectioned to allow modularity. **(G)** Several pyrometer mounting locations – with a pyrometer shown here in the center – to monitor temperature. **(H)** Inlet choke to allow entering gas stream without leaking microwaves. **(I)** Exit choke to allow gas to exit without leaking microwaves.

S2. Thermal Imaging

Thermal imaging with a thermal camera was used to evaluate the radial temperature gradients of the reactor (**Figure S2**). The location of the catalyst bed was marked in the beginning of the experiment using cursors available in FLIR's ResearchIR software. It is immediately evident that the thermal images become increasingly distorted at more extreme operating conditions (**Figure S2a**), owing to the change in emissivity of quartz – a microwave transparent material used to hold the catalyst bed in the reactor – with temperature. When at a slightly elevated temperature (just above 40°C), the catalyst bed is clearly identifiable: the red/orange colored region is the catalyst bed and the blue region is the quartz tube (the blue region is larger at the top of the image since the camera was slightly off-center). As the catalyst bed heats significantly (to above 350°C, past the FLIR camera sensor limit), red colored regions start to appear in a non-uniform pattern in the region previously identified to be the quartz tube. Given the irregularity of this hot region, this effect is most likely the result of reflections; such reflections can complicate imaging analysis. This effect can be made worse at higher flow rates, where thermal transport through higher amounts of fast-moving gas particles adds significant visual distortions. This is evident in **Figure S2b**, where flow rate of unreacting N_2 gas is varied from 1 slm to 6 slm while temperature remains constant. The catalyst bed region is marked initially with cursors as well as an ellipse to denote its true location. As the flow rate gets larger and larger, the image seems to indicate that either the catalyst bed had moved or the reactor setup had rotated with respect to the camera, neither of which had happened. These distortions at extreme operating conditions create anomalies that could lead to false analysis.

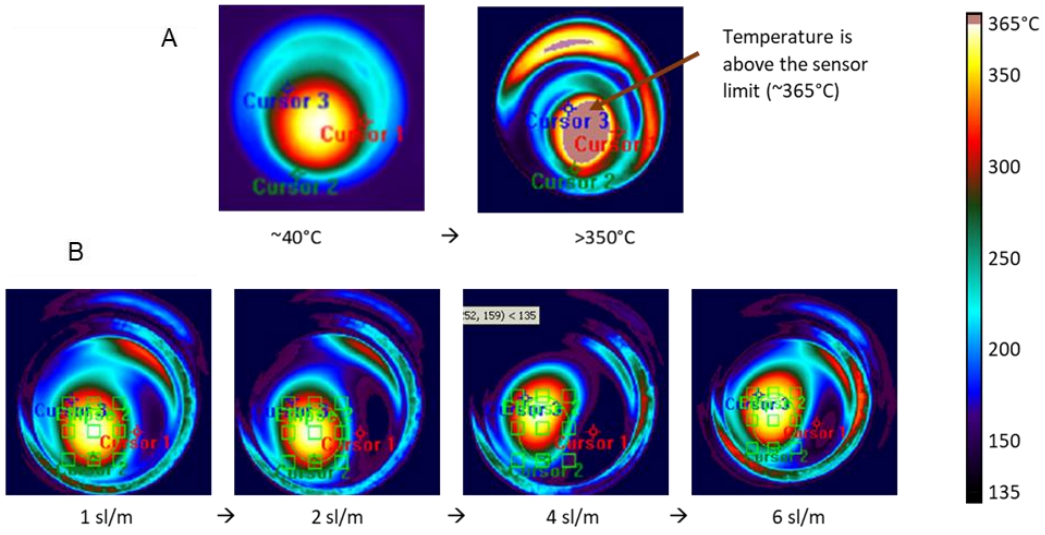

Figure S2. (A) FLIR imaging of 10 g CsRu2-4%/CeO_2 in a 26 mm diameter tube. Flow rate of N_2 gas is maintained at 1 slm, and temperature is increased from about 40°C to about 360°C. **(B)** Temperature is maintained at 260°C while flow rate of N_2 gas is varied between 1 slm and 6 slm.

S3. Dielectric Properties

Dielectric Constant, Loss Index, and Loss Tangent

The real portion (the dielectric constant ε′) and the imaginary portion (the loss index ε″) of complex permittivity can be deduced through experimental measurements. The loss tangent is given by **Equation S1**, a ratio of the loss index to the dielectric constant.

$$tan\delta = \frac{\varepsilon''}{\varepsilon'} \qquad \text{Eq. S1}$$

Attenuation Factor

The attenuation factor (α) of a material is dependent on its loss tangent, in addition to the wavelength (λ) of the electromagnetic field (**Equation S2**).

$$\alpha = \frac{2\pi}{\lambda}\sqrt{\frac{\varepsilon'}{2}\left(\sqrt{1+\left(\frac{\varepsilon''}{\varepsilon'}\right)^2}-1\right)} = \frac{2\pi}{\lambda}\sqrt{\frac{\varepsilon'}{2}\left(\sqrt{1+\tan^2\delta}-1\right)} \qquad \text{Eq. S2}$$

Penetration Depth

It is common practice to report "half-power penetration depth," or the depth at which half of the field has been attenuated, as the "penetration depth" of a material, because field attenuation can be assumed to be uniform below this limit. As such, "half-power penetration depth" will simply be referred to as "penetration depth" throughout this work. Half-power penetration depth (*P*) is proportional to the inverse of attenuation, and it is given by **Equation S3**.

$$P = \frac{ln2}{2} * \alpha^{-1} \qquad \text{Eq. S3}$$

S4. Schematic Illustration of Field Attenuation

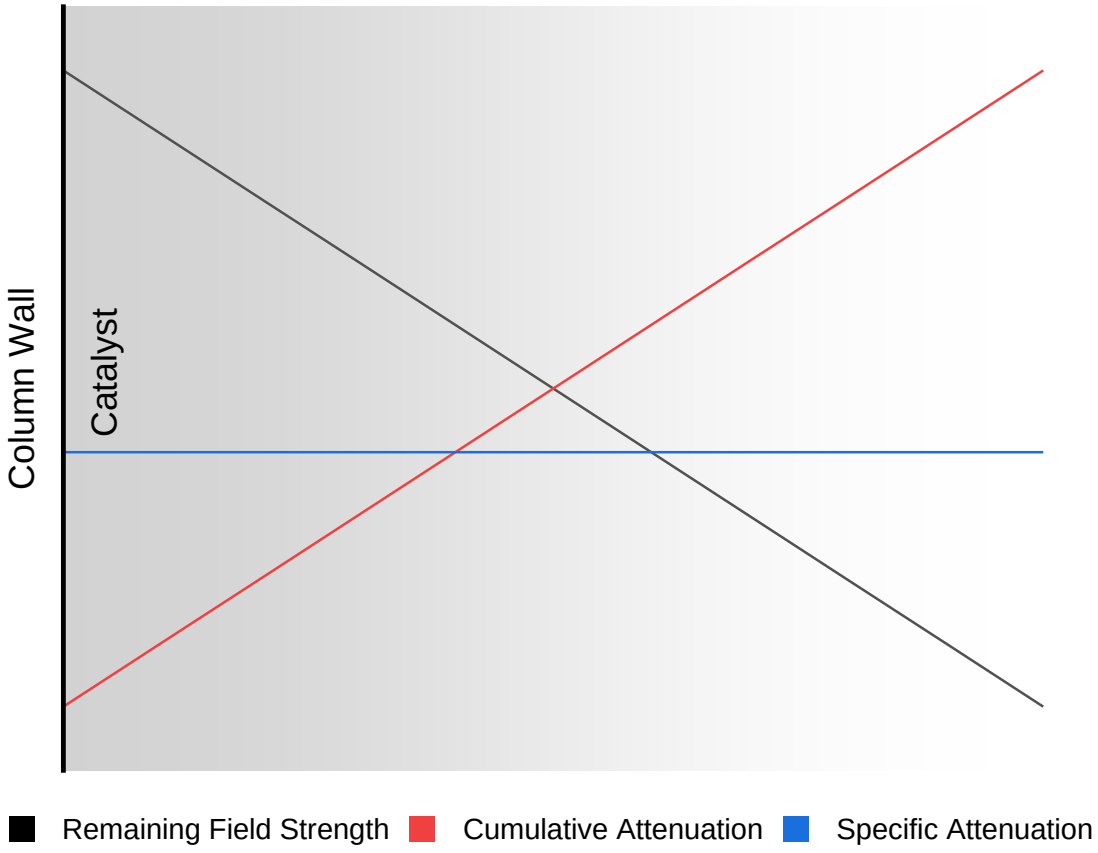

Figure S3. Schematic representation of microwave field attenuation through a catalyst column. Field strength (black line) is strongest at the column wall, the first point of incidence of the microwave field. As the field progressively penetrates inward, microwaves are absorbed into the column and field strength decreases. Specific attenuation (blue line), or the attenuation at a specified point in the column, ideally remains constant. As a result, cumulative attenuation (red line) constantly increases.

S5. Original COMSOL Results

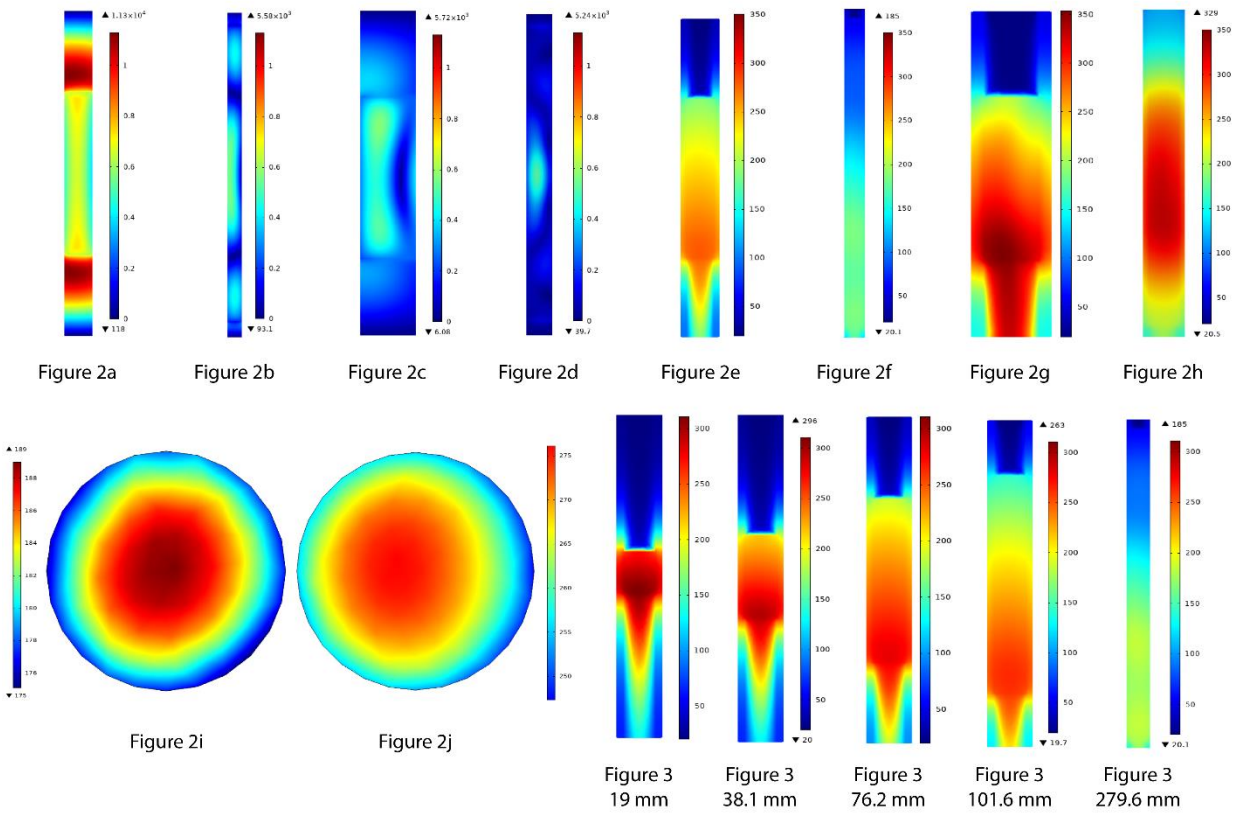

Figure S4. Original COMSOL model results, corresponding to respective parts of **Error! Reference source not found.** and **Error! Reference source not found.**.

S6. Gas Flow Rate Modeling

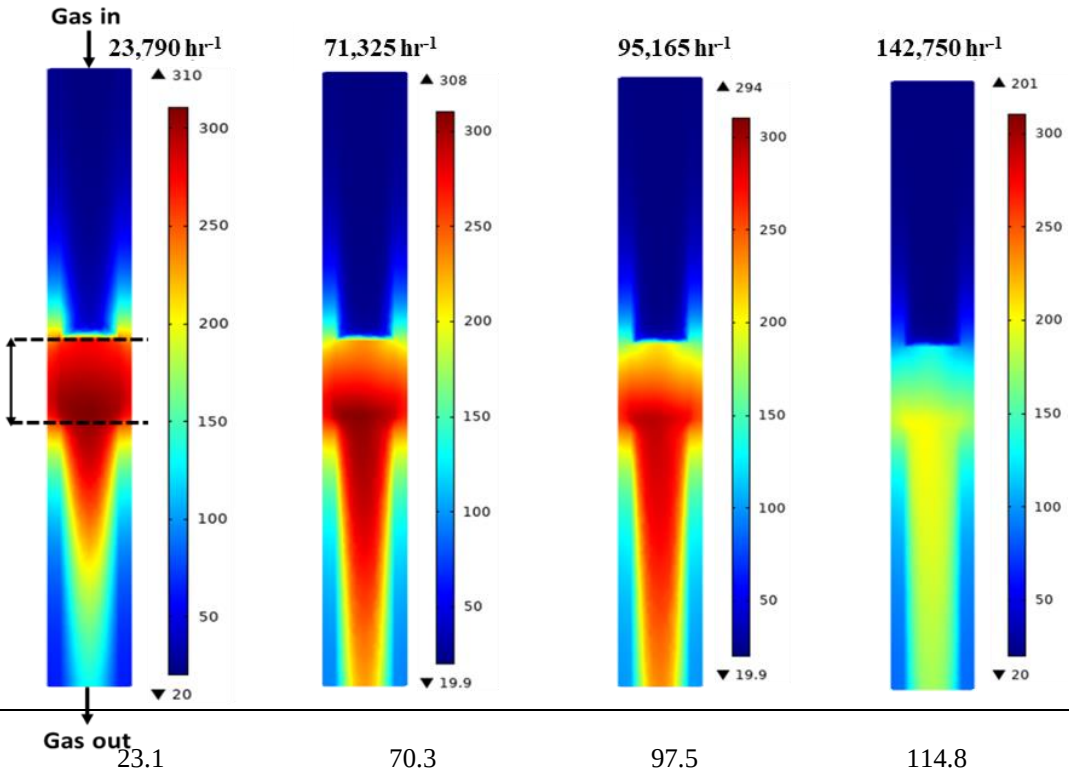

	23,790 hr^{-1}	71,325 hr^{-1}	95,165 hr^{-1}	142,750 hr^{-1}
Absorbed Power (W)	23.1	70.3	97.5	114.8
Minimum Temperature (°C)	251.19	185.05	170.88	102.43
Maximum Temperature (°C)	310.48	288.57	294.49	204.28
Average Temperature (°C)	289.34	245.00	241.30	157.94

Figure S5. Temperature profiles for a 19 mm tall bed in a 13 mm diameter tube with a constant field strength and increasing gas flow rate (GHSV). The corresponding maximum, minimum, and average volumetric temperature of the catalyst beds, as well as the total absorbed power, are also reported.

S7. Variation of Modeled Temperature Profile with Bed Height

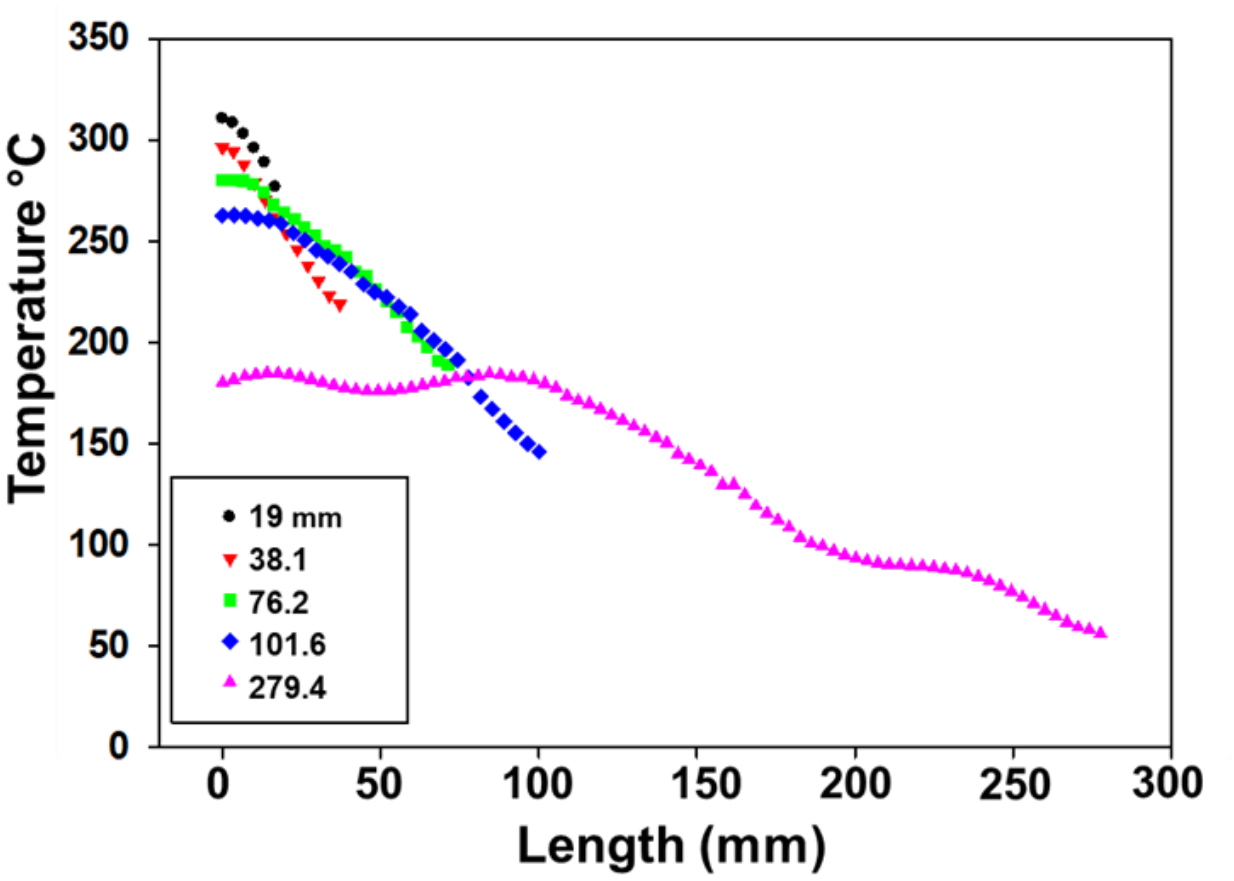

Figure S6. Corresponding to models in **Error! Reference source not found.**, variation of temperature along the length of modeled catalyst beds at different heights (19 mm, 38.1 mm, 76.2 mm, 101.6 mm, 279.4 mm), with the outlet at 0 mm. Gas flow rate was maintained at 1 slm.

S8. Stefan-Boltzman Law of Radiation

The Stefan-Boltzmann Law of Radiation is defined by **Equation S4**.

$$q_{radiation} = \sigma A_1 \varepsilon (T_1^4 - T_2^4) \quad \text{Eq. S4}$$

Where $q_{radiation}$ is the rate of energy emission from the surface of thermal mass 1, σ is Stefan-Boltzmann constant, A_1 is the surface area of thermal mass 1, ε is the emissivity of thermal mass 1, and T_1 and T_2 are the temperatures of thermal mass 1 and thermal mass 2, respectively. The catalyst bed can be considered a cluster of thermal masses that undergo heat transfer with each other, but the bulk catalyst bed also undergoes heat transfer with its surroundings. Temperature has a significantly greater contribution to radiation from a body (4^{th} power) than surface area (linear).

S9. Variation of Conversion and Activity with Space Velocity

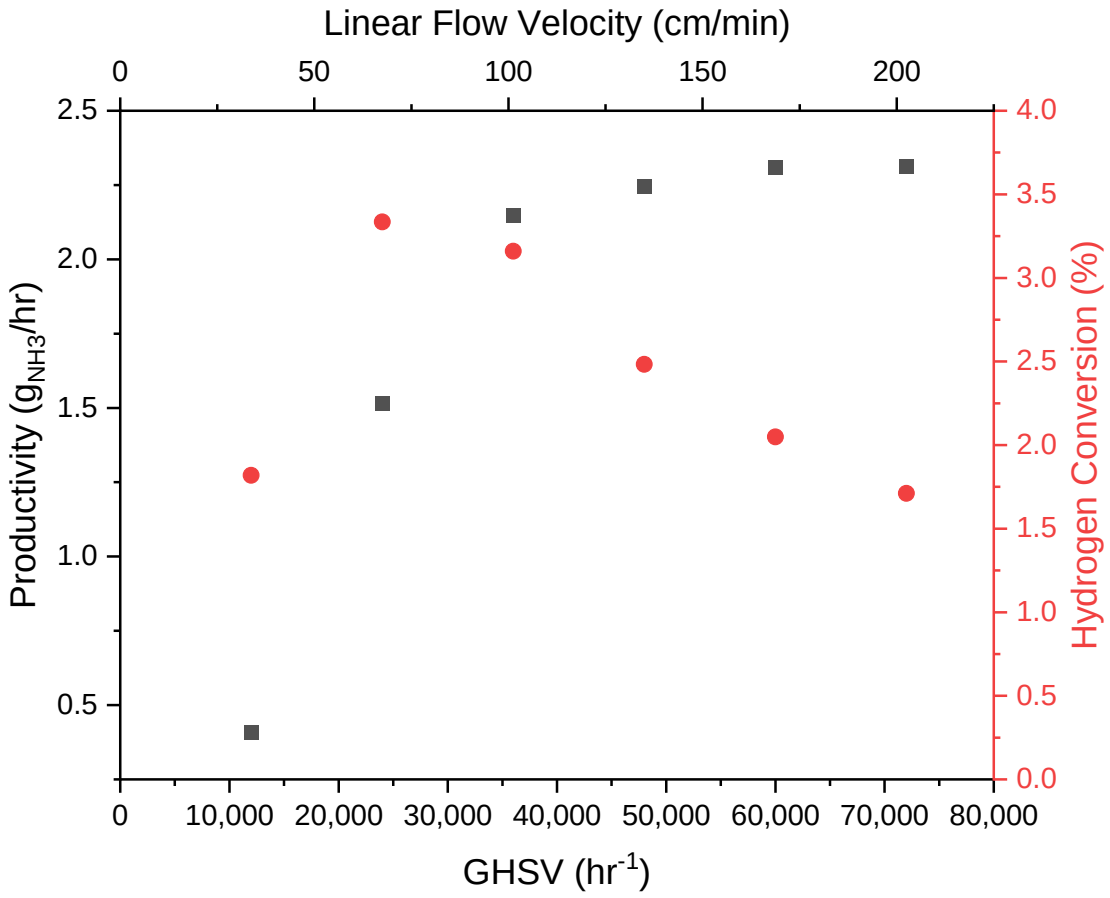

Figure S7. A 10 g catalyst bed loaded into a 13 mm quartz tube and heated to 260°C under microwave irradiation (2450 MHz frequency) at 22 bar. Flow rate of stoichiometric reactant gas (H_2:N_2) varied, with volumetric flow rate on the lower x-axis and the corresponding linear flow velocity on the upper. Conversion first increases with GHSV, as does catalyst productivity. However, conversion decreases while activity continues to increase, before plateauing at the kinetically limited point.

S10. Energy Efficiency Determination

Energy efficiency (*Eff*) was used to determine the productivity of each unit of microwave power (g_{NH3}/kWh). *Eff* was calculated using **Equation S5**, where $\dot{m}_{f,NH_3}$ represents the mass flow rate of ammonia out of the reactor and P_{MW} represents the microwave power required to maintain the given reactor temperature at steady state.

$$Eff = \frac{\dot{m}_{f,NH_3}}{P_{MW}} \quad \text{Eq. S5}$$

S11. Output Analysis

Series	GHSV ($\times 10^4$ hr^{-1})	Temperature (°C)	Pressure (bar)	Microwave Power (W)	Conversion (%)
A	1.0	260	23	25	1.82%
A	2.0	260	23	38	3.37%
A	3.0	260	23	48	3.19%
A	5.0	260	23	61	2.50%
A	6.0	260	23	73	2.06%
A	7.0	260	23	89	1.71%
B	4.0	240	23	39	1.98%
B	4.0	250	23	40	2.07%
B	4.0	260	23	41	2.27%
B	4.0	280	23	43	2.52%
B	4.0	300	23	48	2.53%
B	4.0	320	23	49	2.49%
C	3.3	26	1	35	0.84%
C	3.3	26	8	35	1.15%
C	3.3	26	14	34	1.75%
C	3.3	26	20	33	2.18%
C	3.3	26	23	33	2.33%

Table S1. Microwave power (W) and H_2 conversion (%) for the conditions presented in **Error! Reference source not found.**. Series A varies GHSV ($\times 10^4$ hr^{-1}), B varies temperature (°C), C varies pressure (bar).

S12. Numerical Modeling Details

Governing equations

The governing equation for electromagnetic wave propagation in a medium is given by Maxwell's equations. A wave equation for the electric field distribution in a rectangular waveguide is given by **Equation S6** below.

$$\nabla \times (\frac{1}{\mu^{'}} \times \vec{E}) - \frac{\omega^2}{c} * (\varepsilon^{'} - j\varepsilon^{''})\vec{E} = 0 \quad \text{Eq. S6}$$

Total volumetric power generation due to microwave is deduced from **Equation S7**.

$$Q_{gen} = \sigma_e E^2 = 2\pi f \varepsilon_0 \varepsilon^{''} {E_{rms}}^2 \quad \text{Eq. S7}$$

Where, Q_{gen} is power absorbed from microwave, which is used as a heat generation term in Fourier equation (W/m^3), σ_e is the conductivity (S/m), f is the frequency (Hz).

Heat transfer in porous media is given by **Equation S8**.

$$(\rho C_p)_{eq} \frac{\delta T}{\delta t} + \rho C_p u \cdot \nabla T = \nabla \cdot (k_{eq} \nabla T) + Q_{gen} \quad \text{Eq. S8}$$

Where ρ and Cp are the fluid density and heat capacity of the fluid, whereas $(\rho C_p)_q$ is defined as the equivalent volumetric heat capacity at constant pressure. K_{eq} is the equivalent thermal conductivity, u is defined as the Darcy's velocity expressed as volume flow rate per unit cross sectional area; Q_{gen} is the heat source from electromagnetic heating. The equivalent terms are related to the respective property of the solid and the fluid. Thus, k_{eq} is the equivalent solid-fluid conductivity given by **Equation S9**, and the volumetric heat capacity for solid-fluid system is given by **Equation S10**.

$$k_{eq} = \theta_s k_s + \theta_L k \quad \text{Eq. S9}$$

$$(\rho C_p)_{eq} = \theta_s \rho_s C_s + \theta_L L_p C_p \quad \text{Eq. S10}$$

Where, $\theta_s + \theta_L = 1$ Where, θ_s and θ_L are volume fractions of solid and fluid (porosity) material respectively.

Boundary conditions

Electromagnetic Waves: The electromagnetic waves, frequency domain was used to model the electromagnetic field in the microwave cavity. The microwave power was set based on the study and was varied from 23 W to 100 W depending on the desired temperature. A continuity boundary condition was applied to all the internal boundaries of the domains. An effective medium was defined in catalyst bed domain to account for the porosity of the catalyst bed. The effective media was modeled for catalyst material

(porosity 0.3) and air. Dielectric properties of the catalyst bed were measured and incorporated in the model. Scattering boundary conditions were defined at the outlet and inlet of the quartz tube to avoid undesired reflections and perturbations in the field caused by sudden discontinuity in the waveguide.

Conjugate Heat Transfer: Conjugate heat transfer equations were coupled with the electromagnetic domain and solved in the reactor tube and catalyst bed. The catalyst bed was modeled as a porous media with porosity measured as 0.3. A convective heat flux boundary was defined at the outer walls of the reactor tube to account for the convection cooling. The heat flux was set to 5 W/m^2-K and the external temperature was set at room temperature (20°C). Radiative losses were accounted by defining the surface-to-ambient radiation at the outer walls of the glass tube. The ambient temperature was set to 20°C, and the surface emissivity was measured as 0.92. The heat source Q_{gen} was set as the electromagnetic power loss density calculated from electromagnetics module.

Free and Porous Media Flow: The laminar flow module was active in the quartz tube only. The inlet velocity of the fluid was determined based on the inlet gas flowrates. The inlet gas temperature was set at 20°C. fluid and matrix properties were defined in the catalyst bed and the measured catalyst porosity (0.3) was considered uniform across the bed.

Mesh Generation: The element size requirement for solving the electromagnetic problem is that the maximum grid element size (S_{max}) should be less than half the wavelength. This requirement is known as the Nyquist criterion and is defined by **Equation S11**, where λ is the wavelength (m), f is the frequency (Hz), c is the speed of light in vacuum (m/s), ε′ is the relative dielectric constant, and μ′ is the relative permeability. Based on this criterion, the default fine mesh size was used where the maximum element size was set conservatively at 2.90 mm in the waveguide and the maximum element size was set to 0.89 mm for fluid flow and porous media flow. A coarser mesh was used for waveguide domain which solved for electromagnetic heating only with maximum element size 44.70 mm and minimum size of 3.25 mm. The frequency domain was used to solve the wave equation in the radio frequency module. The frequency was set to 2.45 GHz, which is the operating frequency of the microwave. The fully coupled stationary solver was used to solve heat transfer and fluid flow equations in free and porous media.

$$S_{max} < \frac{\lambda}{2} = \frac{c}{2f\sqrt{\varepsilon'\mu'}} \qquad \text{Eq. S11}$$

S13. Pressure Drop Evaluation

Pressure drop was measured in a catalyst bed while varying gas flow rate, operating pressure, bed temperature, and catalyst particle size (**Figure S8**).

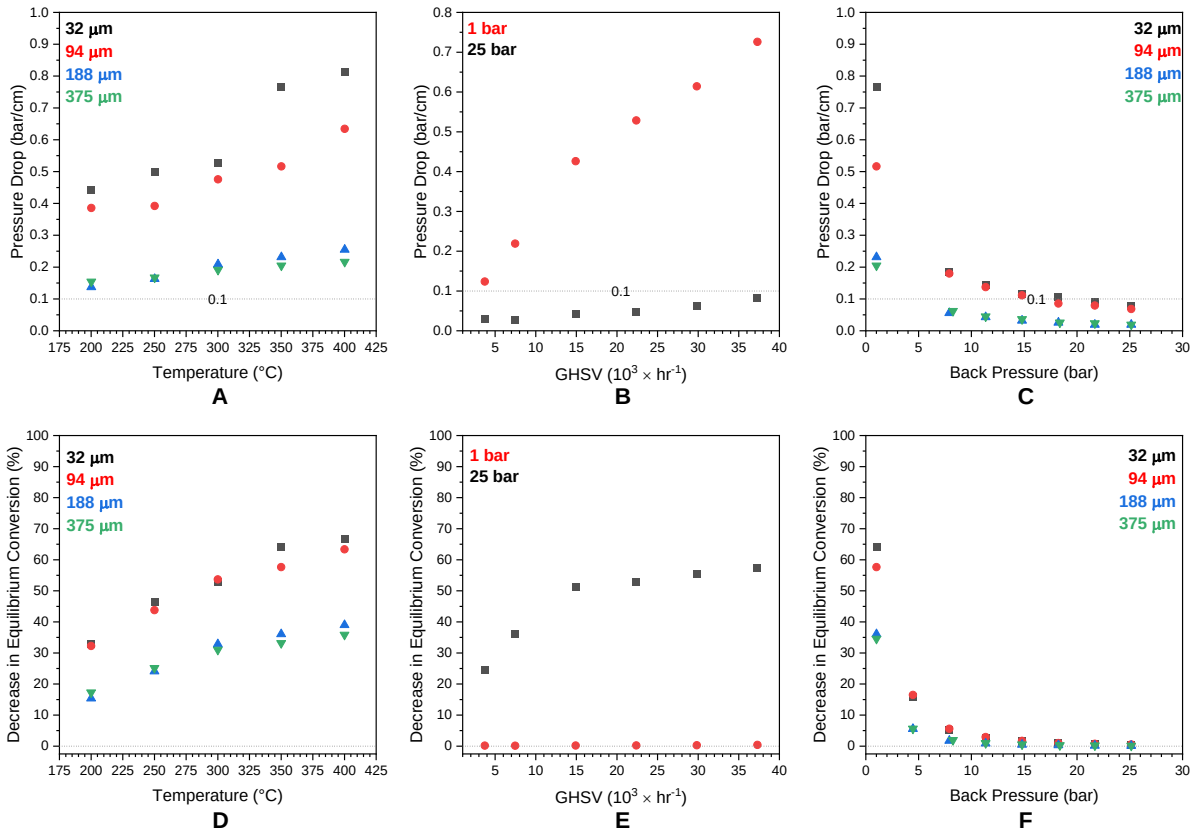

Figure S8. Measured pressure-drop for packed beds of CsRu2-4%/CeO_2. **(A)** Process temperature (°C) was varied through microwave heating, while flow rate (GHSV) and pressure were fixed at about 22,000 hr^{-1} and 1 bar, respectively. Beds of four different average particle diameters were used: 32 µm (black squares), 94 µm (red circles), 188 µm (blue upward triangles), and 375 µm (green downward triangles). **(B)** Flow rate, measured by GHSV (hr^{-1}), was varied for a bed of 32 µm-diameter particles held at a temperature of 300°C. Two operating pressures were tested: 1 bar (red circles) and 25 bar (black squares). **(C)** Back pressure (bar) was varied while GHSV was held at 22,000 hr^{-1} and temperature was held at 350°C. Beds of four different average particle diameters were used: 32 µm (black squares), 94 µm (red circles), 188µm (blue upward triangles), and 375 µm (green downward triangles). **(D)**, **(E)**, and **(F)** show the percent reduction in equilibrium H_2 conversion to ammonia as a result of the reduction in pressure (i.e., the percent difference between equilibrium conversion at the outlet pressure and inlet pressure) found in the conditions depicted in parts **(A)**, **(B)**, and **(C)**, respectively.

Figure S8a shows measured pressure drop (in bar lost per cm of catalyst) as a function of microwave-heated bed temperature (°C) in beds of 4 different average CsRu2-4%/CeO_2 catalyst particle sizes (375 µm, 188 µm, 94 µm, 32 µm), at a constant flow rate (22,000 hr^{-1}) and pressure (1 bar). Temperature is shown to have a slight impact on pressure drop (in the tested range of 200°C – 400°C), where pressure drop increases with temperature. Comparatively, particle size has a greater impact than temperature: beds with smaller particles exhibit significantly greater pressure drops. Regardless, reactor performance can be significantly hampered at this back pressure, as equilibrium H_2 conversion to NH_3 can reduce by as much as 67% depending on the conditions (**Figure S8d**). **Figure S8b** shows the impact of flow rate (in terms of GHSV) on pressure drop at 2 different operating back pressure setpoints (1 bar and 25 bar), with bed temperature set to 300°C and average particle size to 32 µm. Greater flow rates result in larger pressure drops. More significantly, the bed operating at 25 bar showed significantly lower losses in pressure, with all pressure drop values at less than 0.1 bar/cm lost and virtually no change in equilibrium conversion (**Figure S8e**). **Figure S8c** looks further into this influence of operating pressure on pressure drop, where pressure drop is measured at a bed temperature of 350°C and a GHSV of around 22,000 hr^{-1} for 4 different particle size beds (375 µm, 188 µm, 94 µm, 32 µm). Consistent with **Figure S8a**, beds with smaller particle sizes experience greater pressure drops at all conditions tested. Importantly, pressure drop decreases significantly at higher back pressures: measured pressure drop above 20 bar (this work's target operating range) is below 0.1 bar/cm lost in all cases, corresponding to a negligible (less than 1%) change in equilibrium ammonia conversion (**Figure S8f**). Based on this data, the worst conditions for controlling pressure drop are primarily dictated by low operating pressures, with lesser but significant impacts from high gas flow rates and smaller particles (confirmed by a general correlation analysis presented in **Table S2**). Thus, provided operating pressure in this work is set to be above 20 bar with the largest allowable particle sizes, pressure drop is largely not a concern for the scope of this work.

Table S2. Correlation (measured by r-value) between the varied parameters and measured pressure drop, sorted by the largest absolute correlation.

Parameter	r-value
Operating Pressure	-0.66
Flow Rate (GHSV)	0.29
Catalyst Particle Size	-0.26
Bed Temperature	-0.06